

Super-Ionic Conductivity in ω -Li₉TrP₄ (Tr = Al, Ga, In) and Lithium Diffusion Pathways in Li₉AlP₄ Polymorphs

Tassilo M. F. Restle, Stefan Strangmüller, Volodymyr Baran, Anatoliy Senyshyn, Holger Kirchhain, Wilhelm Klein, Samuel Merk, David Müller, Tobias Kutsch, Leo van Wüllen, and Thomas F. Fässler*

Phosphide-based compounds are promising materials for solid electrolytes. In recent times, a multiplicity of compounds featuring isolated MP₄ (M = Si, Ge, Sn, Al, Ga) tetrahedra as structural building units in different arrangements with superionic lithium conductivity have been discovered. ω -Li₉AlP₄, ω -Li₉GaP₄, and ω -Li₉InP₄ are presented as new high-temperature modifications with superionic lithium conductivity reaching 4.5 mS cm⁻¹ at room temperature. Impedance spectroscopy and static temperature-dependent ⁷Li NMR experiments reveal conductivity values in the range of 0.2 to 4.5 mS cm⁻¹ at room temperature and low activation energies for the title compounds. X-ray and neutron diffraction methods disclose that the phosphorus atoms form a cubic-close packing. The triel element and Li atoms are located in tetrahedral voids, further Li atoms partially fill the octahedral voids. Temperature-dependent neutron diffraction shows for Li₉AlP₄ a phase transition at 573 K that influences the occupation of voids with Li and significantly affects the Li-ion mobility. The evaluation of nuclear scattering densities by the maximum-entropy approach and application of the one-particle-potential formalism reveal 3D lithium diffusion with a low activation energy preferentially on paths of adjacent tetrahedral and octahedral voids. The investigation of different polymorphs suggests that the equilibrated filling of tetrahedral and octahedral voids is a crucial parameter for the enhancement of superionic lithium conductivity.

benefits of ASSLIBs are their enhanced safety combined with high energy/power density and mechanical stability.^[1-7] The development of solid electrolytes as key materials in all-solid-state batteries exhibiting high lithium ion diffusion, electrochemical stability, and easy accessibility incites many research groups. So far, a multitude of different material classes have been proven to act as good lithium ion conductors.^[2,5,6] Especially sulfide- and oxide-based materials are nowadays in the focus of research.


The benefit of sulfide-based materials as solid-state ion conductors is that they show quite high ionic conductivities and are mechanically more compressible than oxides.^[8-15] Structurally, the sulfide-based materials can be traced back to the prototype Li₃PS₄.^[16] The pristine compound consists of lithium cations and tetrahedral [PS₄]³⁻ anions and shows in the crystalline γ -modification a rather low conductivity of $\sigma_{\text{Li}} = 3 \times 10^{-7}$ S cm⁻¹ at room temperature (Figure 1).^[17] Related sulfide-based materials can structurally be derived by the introduction of a second type of anion

such as GeS₄⁴⁻, S²⁻, and Cl⁻ which due to their different charges will afford a different number of lithium cations for charge compensation. Several representatives with a significantly higher ionic conductivity are reported. Compounds of the Li-argyrodite

1. Introduction

All solid-state lithium-ion batteries (ASSLIBs) have the potential to outperform state-of-the-art liquid-based batteries. The

T. M. F. Restle, S. Strangmüller, W. Klein, S. Merk, D. Müller, L. van Wüllen, T. F. Fässler
Department of Chemistry
Technical University of Munich
Chair of Inorganic Chemistry with Focus on Novel Materials
Lichtenbergstraße 4, D-85747 Garching, Germany
E-mail: thomas.faessler@lrz.tum.de

 The ORCID identification number(s) for the author(s) of this article can be found under <https://doi.org/10.1002/adfm.202112377>.

© 2022 The Authors. Advanced Functional Materials published by Wiley-VCH GmbH. This is an open access article under the terms of the Creative Commons Attribution License, which permits use, distribution and reproduction in any medium, provided the original work is properly cited.

DOI: 10.1002/adfm.202112377

V. Baran, A. Senyshyn, L. van Wüllen
Research Neutron Source Heinz Maier-Leibnitz (FRM II)
Technical University of Munich
Lichtenbergstraße 1, D-85748 Garching, Germany
H. Kirchhain
Department of Physics
University of Augsburg
Universitätsstraße 1, D-86159 Augsburg, Germany
S. Merk, T. Kutsch
TUMInt.Energy Research GmbH
Lichtenbergstraße 4, D-85747 Garching, Germany

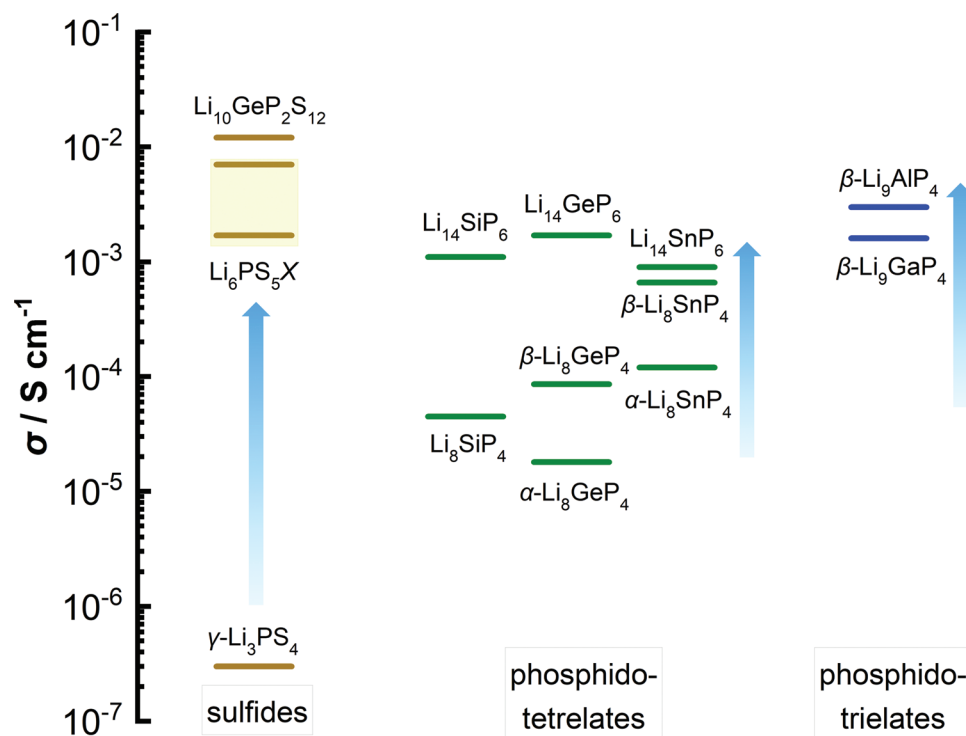


Figure 1. A collection of lithium ion-conducting materials in the class of sulfides (brown), phosphidotetrelates (green) and phosphidotrirelates (blue).

family $\text{Li}_6\text{PS}_5\text{X}$ ($\text{X} = \text{Cl}, \text{Br}, \text{I}$) contain beside $[\text{PS}_4]^{3-}$ also the anions S^{2-} and X^- according to the formula $(\text{Li}^+)_{10}([\text{PS}_4]^{3-})(\text{S}^{2-})(\text{X}^-)$ or $\text{Li}_6\text{PS}_5\text{X} = \text{Li}_3\text{PS}_4 \times \text{Li}_2\text{S} \times \text{LiX}$.^[18] Their ionic conductivity is in the range between 10^{-3} and 10^{-2} S cm^{-1} (Figure 1).^[19,20] A high Li^+ conductivity of 1.2×10^{-2} S cm^{-1} at room temperature (Figure 1) has been reported for undoped $\text{Li}_{10}\text{GeP}_2\text{S}_{12}$ (LGPS) comprising the anions $[\text{PS}_4]^{3-}$ and $[\text{GeS}_4]^{3-}$ according to the formula $(\text{Li}^+)_{10}([\text{PS}_4]^{3-})_2([\text{GeS}_4]^{4-})$ or $\text{Li}_{10}\text{GeP}_2\text{S}_{12} = 2 \text{Li}_3\text{PS}_4 \times \text{Li}_4\text{GeS}_4$.^[21] Even higher ionic conductivities were obtained upon the substitution of S^{2-} by halides.^[15] Ionic conductivities up to 10^3 S cm^{-1} have also been reported for the closely related *thio*-LISICONS.^[22–25]

In recent years, a new solid-state ion conducting compound family with related tetrahedral building blocks has been introduced. This material class is based on iso-valence-electronic tetrahedral units with phosphorus instead of sulfur atoms, thereby creating one additional negative charge per P atom and consequently with more lithium ions in the structure. The first reported compound of this family is the phosphidosilicate Li_8SiP_4 , that is composed by Li^+ and $[\text{SiP}_4]^{8-}$ tetrahedra. The ionic conductivity of Li_8SiP_4 with $\sigma_{\text{Li}} = 6 \times 10^{-6}$ S cm^{-1} at ambient temperature is more than one order of magnitude higher than that of $\gamma\text{-Li}_3\text{PS}_4$.^[26,27] Even higher ionic conductivities up to 1.2×10^4 S cm^{-1} have been detected for the heavier homologs, the phosphidogermanates and phosphidostannates Li_8GeP_4 or Li_8SnP_4 . The latter compounds exist in two different structure modifications, named as “ α ” (isotypical with Li_8SiP_4) and “ β ”. The β modifications (space group $P43n$) show significantly higher ionic conductivities than the respective α modifications (space group $P\bar{a}3$).^[27,28] As in sulfide-based materials, the introduction of a second anion type such as P^{3-}

led to novel compounds, here with the composition $\text{Li}_{14}\text{SiP}_6$, $\text{Li}_{14}\text{GeP}_6$, and $\text{Li}_{14}\text{SnP}_6$, whose formula can be rewritten as $(\text{Li}^+)_{14}([\text{TiP}_4]^{8-})(\text{P}^{3-})_2$ or $\text{Li}_{14}\text{TiP}_6 = \text{Li}_8\text{TiP}_4 \times 2 \text{Li}_3\text{P}$ with $\text{Ti} = \text{Si}, \text{Ge},$ and Sn .^[29,30] Along with a larger amount of lithium and an increasing structural complexity higher ionic conductivities up to 1.7×10^{-3} S cm^{-1} were observed.^[29,30] An overview of the ionic conductivities is presented in Figure 1.

The highest lithium-ion conductivity of the phosphide-based materials was recently reported for the related lithium phosphidoaluminate Li_9AlP_4 , which is composed of Li ions and $[\text{AlP}_4]^{9-}$ tetrahedra.^[31] The lithium phosphidoaluminate exhibits an ionic conductivity of 3×10^{-3} S cm^{-1} at ambient temperature and, thus, approximately two and four orders of magnitude higher than Li_8SiP_4 and $\gamma\text{-Li}_3\text{PS}_4$, respectively (Figure 1).^[31] Li_9AlP_4 is isotypic to $\beta\text{-Li}_8\text{GeP}_4$ according to the arrangement of the AlP_4 or GeP_4 tetrahedra, respectively. Although, in contrast to Li_8GeP_4 , the α structure type, exhibiting a different arrangement of the tetrahedral anions, has not been found to date, Li_9AlP_4 is assigned to the β type to emphasize the structural relationship. The isotypic subsequently reported $\beta\text{-Li}_9\text{GaP}_4$ exhibits an ionic conductivity of 1.6 mS cm^{-1} (Figure 1).^[32] The higher amount of lithium atoms which is necessary to balance the higher charge of the tetrahedral anions in $\beta\text{-Li}_9\text{AlP}_4$ and $\beta\text{-Li}_9\text{GaP}_4$ as compared to $\beta\text{-Li}_8\text{GeP}_4$ or $\beta\text{-Li}_8\text{SnP}_4$ leads to a higher degree of occupation of the octahedral sites. Compared to phosphidotetrelates, these changes had been interpreted as an energy landscape flattening that boosts the ionic conductivity.^[31,32]

Phosphidotetrelates with linked tetrahedra and consequently a smaller amount of lithium atoms like $\text{Li}_{10}\text{Si}_2\text{P}_6$, Li_2SiP_2 & Li_2GeP_2 , LiSi_2P_3 , $\text{Li}_3\text{Si}_3\text{P}_7$, and LiGe_3P_3 ^[26,33–35] as well as

phosphidotrirelates such as Li_3AlP_2 , Li_3GaP_2 ^[36] and Li_3InP_2 ^[37] exhibit polyanionic structures with 1-, 2-, and 3D networks of corner- and/or edge-sharing tetrahedra. However, all compounds with polyanionic structures of linked tetrahedra are only poor lithium-ion conductors.

In this work, we perform a comprehensive analysis of the structure and the lithium diffusion pathways in $\beta\text{-Li}_9\text{AlP}_4$ applying powder neutron diffraction experiments. Investigation of the thermal properties of $\beta\text{-Li}_9\text{AlP}_4$ revealed a phase transition from the ordered phase (ordered Li and Al atom position) into a disordered high-temperature phase $\omega\text{-Li}_9\text{AlP}_4$ (statistical distribution of Li and Al). The high-temperature modification crystallizes in the defect Li_3Bi structure type with a high cubic symmetry. Due to the so far two known ordered modifications (α and β) for phosphidotetrelates and -trielates of the composition 8:1:4 and 9:1:4 (Li:M:P) and possibly an unknown number of further ordered modifications by the incorporation of other metals, the high-temperature modification is labeled as “ ω ”-modification. By transferring these results to the heavier triel homologs, $\omega\text{-Li}_9\text{GaP}_4$ and $\omega\text{-Li}_9\text{InP}_4$ with even higher ionic conductivities were obtained.

2. Results

The superionic conductor Li_9AlP_4 crystallizes at ambient temperature with the cubic space group $P\bar{4}3n$ and a lattice parameter of $a = 11.852(1)$ Å. The structure is built up by isolated $[\text{AlP}_4]^{9-}$ tetrahedra surrounded by Li^+ ions (Figure 2a). In an alternative view, the P atoms form a slightly distorted cubic close packing (ccp) and the unit cell corresponds to a $2 \times 2 \times 2$ superstructure with respect to the basic Li_3Bi structure type. The compound in this low-temperature superstructure is labeled as $\beta\text{-Li}_9\text{AlP}_4$. With $Z = 8$, there are 32 P atoms per unit cell, 64 tetrahedral and 32 octahedral voids result. A previously reported single crystal determination showed that at 150 K Al and Li atoms fill all tetrahedral voids up to 91%, whereas surplus Li atoms occupy 58% of the octahedral voids.^[31] Now we

found that at 573 K $\beta\text{-Li}_9\text{AlP}_4$ undergoes a phase transition to the novel polymorph $\omega\text{-Li}_9\text{AlP}_4$. Therefore, we re-examined the structure of $\beta\text{-Li}_9\text{AlP}_4$, and synthesized the high-temperature phase $\omega\text{-Li}_9\text{AlP}_4$ as well as the heavier homologs $\omega\text{-Li}_9\text{GaP}_4$ and $\omega\text{-Li}_9\text{InP}_4$ as bulk materials.

In the following, we describe the synthesis of the new compounds, their physical properties and their structures based on powder X-ray diffraction analyses. $\beta\text{-Li}_9\text{AlP}_4$ and $\omega\text{-Li}_9\text{AlP}_4$ were further studied by neutron diffraction methods including investigations at various temperatures. Based on the nuclear densities from neutron diffraction data a detailed analysis of the lithium migration pathway for the β - and ω -polymorphs of Li_9AlP_4 was carried out using the maximum entropy method.

2.1. Synthesis of $\beta\text{-Li}_9\text{AlP}_4$, $\omega\text{-Li}_9\text{AlP}_4$, $\omega\text{-Li}_9\text{GaP}_4$ and $\omega\text{-Li}_9\text{InP}_4$

$\beta\text{-Li}_9\text{AlP}_4$ was synthesized according to literature by ball milling of the elements and subsequent annealing at 973 K followed by slow cooling to room temperature.^[31] The DSC measurement of the reactive intermediate after ball milling shows an endothermic signal at around 590 K in the first and in the second heating cycle (see Figure S3, Supporting Information). The PXRD after the measurements indicates a phase transformation (Figure S4, Supporting Information). Since there is no exothermic signal during cooling, the phase transformation is already suppressed by cooling with 10 K min^{-1} . Based on the DSC results, phase-pure, brown-yellow $\omega\text{-Li}_9\text{AlP}_4$ could be obtained via ball milling of lithium, aluminum and phosphorus in the ratio 9:1:4 and subsequent annealing in niobium ampules at 973 K for one day, followed by rapid quenching to room temperature in ice/water (Figure 3a).

The heavier gallium and indium homologs were obtained by the same synthetic protocol using ball milling synthesis and subsequent DSC analyses. The DSC measurement of the product after the ball milling procedure of the composition “ Li_9GaP_4 ” shows reversible signals in the first and second cycle at ≈ 520 and 800 K (Figure S5, Supporting Information). The

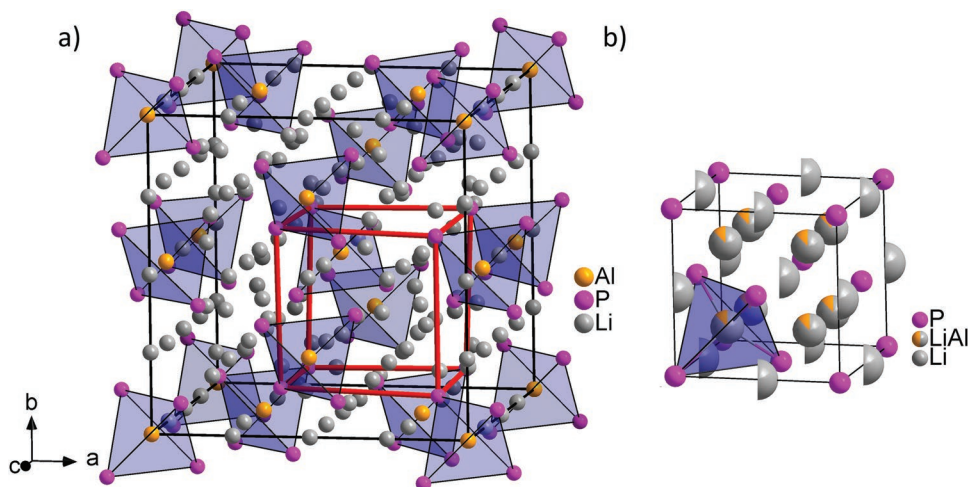


Figure 2. a) Unit cell of $\beta\text{-Li}_9\text{AlP}_4$ as published in standard projection of the atoms.^[31] The face-centered cubic structure of the P atoms is emphasized in red. b) The crystal structure of $\omega\text{-Li}_9\text{AlP}_4$ as determined from neutron data. Li, Al and P are depicted in grey, orange and purple color, respectively (displacement ellipsoids set at 50% at 973 K). According to the statistic, there is one AlP_4 tetrahedron per unit cell.

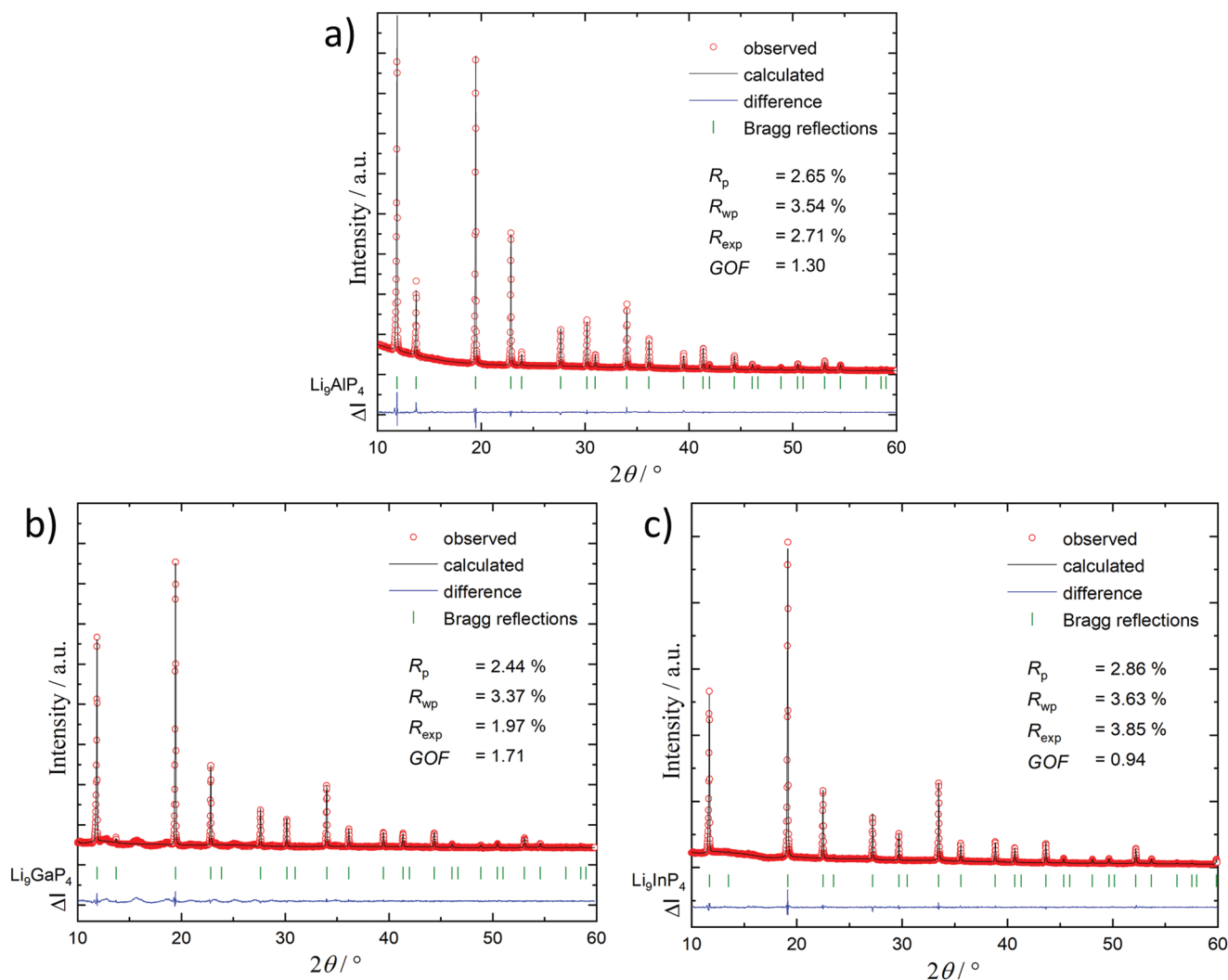


Figure 3. X-ray powder diffractograms of $\omega\text{-Li}_9\text{AlP}_4$, $\omega\text{-Li}_9\text{GaP}_4$, and $\omega\text{-Li}_9\text{InP}_4$. The red, black, and blue lines indicate the observed and the calculated intensities, and the difference between both, respectively. Bragg positions are given in green dashes.

PXRD after the DSC measurements indicates the formation of $\beta\text{-Li}_9\text{GaP}$ (Figure S6, Supporting Information). This is in good accordance with the previous observation that $\beta\text{-Li}_9\text{GaP}_4$ is formed either upon annealing of ball milled “ Li_9GaP_4 ” and subsequent slow cooling to room temperature or upon annealing of “ Li_9GaP_4 ” at 673 K.^[32] The DSC measurement of the product “ Li_9InP_4 ” after ball milling shows two irreversible signals at 425 and 820 K only during the first heating, and during cooling no signals are observed (Figure S7, Supporting Information). After the DSC measurement, the powder X-ray diffractogram of the sample contains only reflections that refer to the novel ω modification (Figure S8, Supporting Information). $\omega\text{-Li}_9\text{InP}_4$ is already formed upon annealing at 673 K and slow cooling, and so far there is no evidence for the existence of the β or any other ordered modification of Li_9InP_4 . Instead, impurities of Li_3InP_2 and LiP occur after annealing at 673 K and subsequent slow cooling besides the main phase $\omega\text{-Li}_9\text{InP}_4$, as confirmed by Rietveld analysis (see Figure S9, Supporting Information). Phase-pure $\omega\text{-Li}_9\text{GaP}_4$ and $\omega\text{-Li}_9\text{InP}_4$ were synthesized applying the same synthesis protocol as described for $\omega\text{-Li}_9\text{AlP}_4$. After

ball milling of stoichiometric amounts of Li, P and the respective triel element, pellets of the product were subsequently annealed in niobium ampules at 973 K for one day, followed by a rapid cooling to room temperature in ice/water (Figure 3b,c). Powdered $\omega\text{-Li}_9\text{GaP}_4$ is light-red, and powdered $\omega\text{-Li}_9\text{InP}_4$ is red-orange.

2.2. Powder X-Ray Diffraction of $\omega\text{-Li}_9\text{AlP}_4$, $\omega\text{-Li}_9\text{GaP}_4$ and $\omega\text{-Li}_9\text{InP}_4$

Since suitable single crystals of the compounds could not be obtained, the crystal structures of $\omega\text{-Li}_9\text{TP}_4$ were solved by Rietveld refinement (Figure 3). For all the isotypic compounds X-ray data were used, additionally for $\omega\text{-Li}_9\text{AlP}_4$, temperature-dependent neutron data were applied. Crystallographic data and results of the Rietveld refinements are given in Table 1 (see also Tables S1–S6, Supporting Information).

The Rietveld analyses of the PXRD measurement at room temperature reveals for all compounds a cubic unit

Table 1. Crystallographic data of ω -Li₉AlP₄, ω -Li₉GaP₄ and ω -Li₉InP₄ obtained from powder X-ray diffraction data by Rietveld refinement.

Empirical formula	Li _{9.16(8)} AlP ₄	Li _{9.24(25)} Ga _{0.96(1)} P ₄	Li _{8.73(13)} In _{0.992(8)} P ₄
Formula weight/g mol ⁻¹	214.46	254.96	298.39
T/K	300		
Radiation wavelength	$\lambda = 0.7093 \text{ \AA}$		
Color	brown-yellow	light-red	red-orange
Crystal system	Cubic		
Space group	$Fm\bar{3}m$ (no. 225)		
Unit cell dimension			
$a/\text{\AA}$	5.94067(4)	5.94324(9)	6.03378(4)
$V/\text{\AA}^3$	209.656(4)	209.928(9)	219.669(5)
Z	1		
ρ (calc.)/g cm ⁻³	1.68346(4)	2.01840(9)	2.23216(5)
θ Range/deg	10.00–60.00	10.00–59.83	10.00–59.92
R_p	0.0265	0.0244	0.0286
R_{wp}	0.0354	0.0337	0.0363
R_{exp}	0.0271	0.0197	0.0385
Goodness-of-fit	1.304	1.71	0.94
Depository no.	CSD-2121628	CSD-2121629	CSD-2121630

cell according to a structure including a *ccp* of P atoms with all tetrahedral voids filled statistically with Li and *Tr* atoms as well as further Li atoms in octahedral voids (Figure 2b). The cell parameters at room temperature are for ω -Li₉AlP₄: $a = 5.94070(4) \text{ \AA}$, for ω -Li₉GaP₄: $a = 5.94324(9) \text{ \AA}$, and for ω -Li₉InP₄: $a = 6.03378(4) \text{ \AA}$. ω -Li₉*Tr*P₄ crystallize in the cubic space group $Fm\bar{3}m$ (no. 225) with three independent crystallographic positions (P1, Li1/*Tr*1, Li2) (Tables S1–S3, Supporting Information). The tetrahedral voids are occupied by a lithium/triel mixed position with a statistical occupancy of one-eighth for the triel element and seven-eighths for lithium. Thus, each unit cell statistically contains one *Tr*P₄ tetrahedron. The octahedral voids are filled to one-half with lithium. The enlarged displacement parameter of the lithium atom in the octahedral void indicates that this void might be too large for the relatively small lithium atom. A large displacement parameter of the octahedral lithium atom was also observed in the related compounds Li₁₄*Ti*P₆ (*Ti* = Si, Ge, Sn).^[29,30] The relation of ω -Li₉*Tr*P₄ to Li₁₄*Ti*P₆ will be discussed in more detail below. The calculated formula obtained from the Rietveld analyses is in good agreement with the expected stoichiometry of ω -Li₉*Tr*P₄. For ω -Li₉InP₄, the formula has been confirmed by a second Rietveld refinement of a sample synthesized at 673 K (Figure S9 and Table S7, Supporting Information).

2.3. Powder Neutron Diffraction Analysis on β - and ω -Li₉AlP₄

Powder neutron diffraction measurements of β -Li₉AlP₄ were performed in a temperature range between 4 and 1000 K. According to the results obtained at 4 K the sample contains up to 5 % LiP as a side-phase. The structure at 4 K is in agreement with that found by single crystal X-ray diffraction (Figure S10, Tables S8 and S9, Supporting Information).^[31]

In the β modification, the aluminum atoms occupy 1/8 of the tetrahedral voids. The resulting AlP₄ tetrahedra are arranged in a way comparable to that in the Cr₃Si structure-type. The lithium atoms partially occupy the remaining tetrahedral (Li1–Li5) and octahedral (Li6a, Li6b, and Li7) voids. In detail, Li1, Li4, and Li5 are fully occupied, whereas Li2 and Li3 are only partially occupied (*sof* Li2: 0.62(3) and Li3: 0.79(3)), and both octahedral voids (24i and 8e) are only partially occupied (*sof* Li6a: 0.47(2), Li6b: 0.22(2) and Li7: 0.42(4)). Overall, the occupation of tetrahedral and octahedral positions by lithium is 81.3 % and 62.3 %, respectively. In the octahedral void 24i the lithium atom appears in a split position (Li6a and Li6b) with a preference of position Li6a. In the octahedral void 8e the lithium position is also only partially occupied, but a split position can not be found. Furthermore, the lithium atoms in the octahedral voids are not located in the center of gravity of the P₆ octahedron, but are shifted toward specific triangular faces of the octahedron, which are shared with LiP₄ tetrahedra of the partially occupied lithium positions Li2 and Li3. BVS calculations based on the Al and P positions support the lithium positions found by neutron diffraction (Figure S12, Supporting Information). Furthermore, the split position and the off-centered positions in the octahedral void are in good agreement with the BVS calculations (Figure S12, 0.2 x *d*, Supporting Information). In summary, the crystal structure and especially the site occupation factors determined by powder neutron diffraction are generally in good accordance with the results previously reported by X-ray single crystal diffraction.^[31] There are rather small differences in the relative degree of filling with Li atoms in octahedral positions (62% by powder neutron and 58% by SC-XRD), whereas the filling of the tetrahedral voids differs slightly (81% by powder neutron and 91% by SC-XRD), which, however, arises from the different methods which were used. In sum, the formula Li_{8.7(2)}AlP₄ (single crystal X-ray diffraction) and Li_{9.0(2)}AlP₄

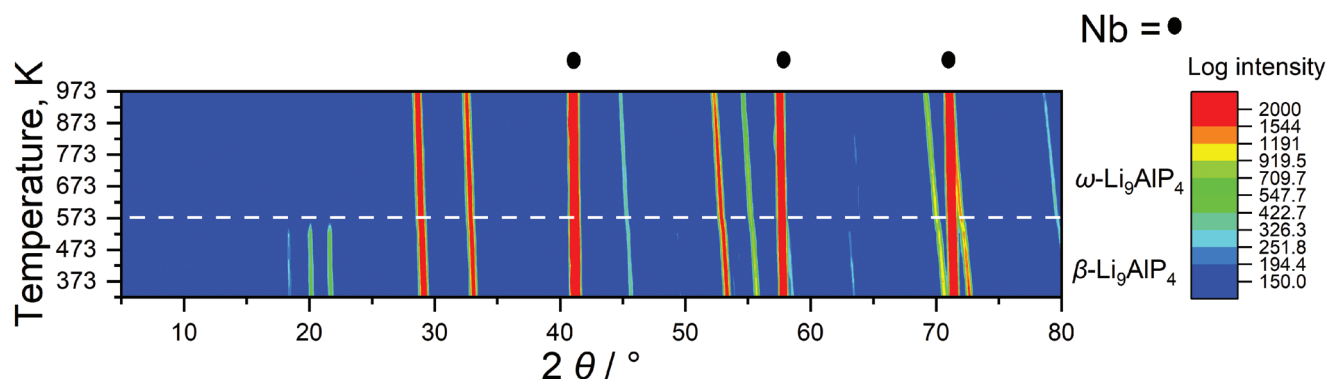


Figure 4. 2D plot of the data of temperature-dependent neutron diffraction measurements from 323 to 973 K in a 2θ range from 5 to 80° (sample sealed in an Nb ampoule under Ar). Around 573 K the ordered phase ($\beta\text{-Li}_9\text{AlP}_4$) transforms into the disordered phase ($\omega\text{-Li}_9\text{AlP}_4$), which is indicated by the loss of the superlattice reflections (e.g., at $20^\circ 2\theta$). The container material Nb is indicated with solid circles.

(neutron powder diffraction) confirm a composition that allows for charge balance.

The powder neutron experiment at 300 K indicates that no phase transformation takes place up to this temperature (Figure S11, Tables S10 and S11, Supporting Information). Acquired neutron powder diffractograms in the temperature range between 323 and 973 K in steps of 50 K reveal a phase transformation from $\beta\text{-Li}_9\text{AlP}_4$ to $\omega\text{-Li}_9\text{AlP}_4$ at around 573 K (Figure 4). The transition is in good accordance with the DSC measurement of $\beta\text{-Li}_9\text{AlP}_4$ (Figure S3, Supporting Information), which shows an endothermic signal shortly above 573 K. At 973 K a neutron powder measurement with longer exposure was performed for $\omega\text{-Li}_9\text{AlP}_4$. During the phase transition, superlattice reflections of $\beta\text{-Li}_9\text{AlP}_4$, e.g., below 20° in 2θ disappear. Indexing the remaining reflections results in a lattice parameter about half as long as the initial cell parameter of $\beta\text{-Li}_9\text{AlP}_4$. As discussed above, $\omega\text{-Li}_9\text{AlP}_4$ crystallizes in the space group $Fm\bar{3}m$ with a lattice parameter of $a = 6.05949(7)$ Å at 973 K.

The temperature dependence of the lattice parameters is plotted in Figure S13 (Supporting Information). Both $\beta\text{-Li}_9\text{AlP}_4$ and $\omega\text{-Li}_9\text{AlP}_4$ show a linear increase of the lattice parameters with increasing temperature and with almost equal slope. However, the normalized cell parameters reveal a discontinuous increase at the transition temperature. Hence, the disordered phase $\omega\text{-Li}_9\text{AlP}_4$ exhibits a slightly larger volume compared to the ordered phase.

The structure of $\omega\text{-Li}_9\text{AlP}_4$ was solved by Rietveld refinement using the structure model of the previously reported $\text{Li}_{14}\text{TiP}_6$ (Figure 5).^[29,30] Complete data of the Rietveld refinement are given in Table 2, and the atomic coordinates are listed in Table 3.

The P atoms form a perfect *ccp* lattice. All resulting tetrahedral voids are statistically filled with Li and Al atoms, and the octahedral voids are partially filled with lithium. Tetrahedral voids are randomly filled by 12.5 % and 87.5 % with Al and Li, respectively, and the octahedral voids are partially occupied by 50 % with Li. The crystal structure of $\omega\text{-Li}_9\text{AlP}_4$ is shown Figure 2b. The lithium atom Li2, which is located at the center of the octahedral voids, has a larger displacement parameter than the Li atoms in the tetrahedral voids, which has already been observed for the related compounds $\text{Li}_{14}\text{TiP}_6$.^[29,30] This could be either related with the increased degree of localized

motion caused by Li by Al substitution at the Li1 site or by the fact that the actual position is not in the center of the 6 P atoms that make up the void, as already described in the above chapter. The observed phase transition to a structure with a smaller lattice parameter (half of the initial cell parameter) than that of the low-temperature modification corresponds to known order-disorder transitions upon temperature increase. However, the disorder affects only the Li and Al positions in tetrahedral voids. $\omega\text{-Li}_9\text{AlP}_4$ corresponds to a defect variant of the Li_3Bi structure, since in Li_3Bi all octahedral sites are completely filled.

The structure type was also observed for the lithium-ion conductors $\text{Li}_{14}\text{TiP}_6$ ($\text{Ti} = \text{Si}, \text{Ge}, \text{Sn}$)^[29,30] which have a statistical occupation of lithium and tetrel element atoms in tetrahedral sites. The group-subgroup relation between the disordered and ordered structure with the space groups $Fm\bar{3}m$ and $P43n$, respectively, was deduced before.^[27] The symmetry degrades from $Fm\bar{3}m$ via $Pn\bar{3}m$, $P43m$ and $I43m$ to $P43n$ by one

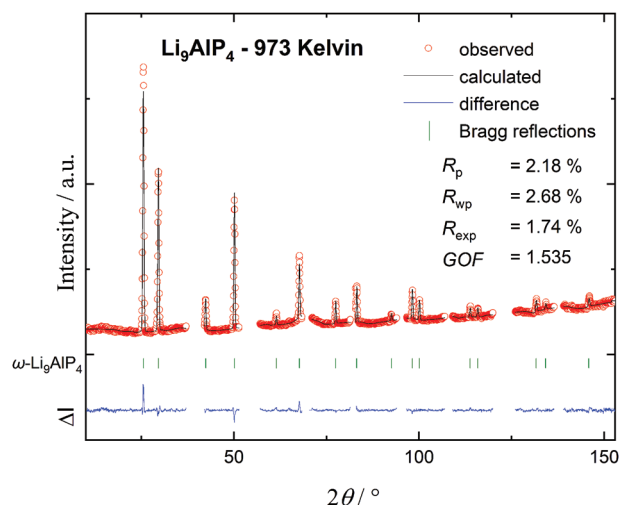


Figure 5. Rietveld analysis of the powder neutron diffractogram of $\omega\text{-Li}_9\text{AlP}_4$ at 973 K. The red line indicates the observed intensities, the black line the calculated intensities and the blue line the difference between both. Bragg positions are marked by green dashes. The regions around reflections of the container material Nb were excluded.

Table 2. Crystallographic data of ω -Li₉AlP₄ obtained from powder neutron diffraction data by Rietveld refinement at 973 K.

Empirical formula	Li ₉ AlP ₄
Formula weight/g mol ⁻¹	213.35
T/K ⁻¹	973
Color	red-brown
Crystal system	Cubic
Space group	<i>Fm</i> $\bar{3}$ <i>m</i> (no. 225)
Unit cell dimension	
<i>a</i> /Å	6.05949(7)
<i>V</i> /Å ³	222.489(5)
<i>Z</i>	1
ρ (calc.)/g cm ⁻³	1.59232
λ /Å	1.5482
θ Range/deg	12.00–151.90
<i>R</i> _p	0.0218
<i>R</i> _{wp}	0.0268
<i>R</i> _{exp}	0.0174
GOF	1.535
depository no.	CSD-2121627

translationsgleichen and three *klassengleiche* transitions including a doubling of the lattice parameters.

2.4. ⁷Li-NMR Spectroscopy

Static ⁷Li NMR spectra of ω -Li₉TrP₄ (*Tr* = Al, Ga, In) were recorded as a function of temperature to study the dynamic behavior of the lithium ions. The central transition of the ⁷Li nucleus (*I* = 3/2) is broadened by the homo (⁷Li–⁷Li) and heteronuclear (⁷Li–³¹P) dipolar interactions, which both scale with the second Legendrian ($3\cos^2\beta-1$). Any fast dynamic process will produce a (partial) averaging of the orientational dependence resulting in a narrowing of the NMR signal. Hence, temperature-dependent ⁷Li NMR measurements can be used to get insights into the local lithium diffusion.

The static ⁷Li spectrum of ω -Li₉AlP₄ (Figure 6a, bottom) displays a homogeneous Lorentzian shape at 290 K. Upon cooling, the signal gradually broadens, evolving to a Gaussian line shape (Figure 6a, top). At intermediate temperatures of 166 and 200 K, the line shape indicates some heterogeneity, which may be related to a distribution of activation energies for the Li

Table 3. Atomic coordinates and site occupancy factors (*sof*) for ω -Li₉AlP₄ from neutron diffraction data by Rietveld refinement at 973 K.

Atom	Wyck.	<i>x</i>	<i>y</i>	<i>z</i>	<i>sof</i>	<i>U</i> _{iso} (neutron)
P1	4a	0	0	0	–	0.0635(4)
Al1	8c	¼	¼	¼	0.125	0.156(2)
Li1	8c	¼	¼	¼	0.875	0.156(2)
Li2	4b	½	½	½	0.50	0.226(6)

ions occupying both tetrahedral and octahedral sites. Individual contributions from the different Li sites in the crystal lattice could not be resolved. For temperatures >234 K a homogeneous line shape is observed, indicating all mobile Li ions. For ω -Li₉GaP₄, the static ⁷Li spectrum (Figure 6c) displays already at 205 K a homogeneous Lorentzian shape. At 165 K, the signal shape shows some heterogeneity, whereas at 125 K the line shape is Gaussian-like. At room temperature ω -Li₉InP₄ displays a homogeneous Lorentzian shape, between 165 and 245 K a heterogeneous line shape and at 125 K a Gaussian line shape (Figure 6e).

The temperature-dependent evolution of the line width (FWHM; full width at half height) of the ⁷Li signal allows for a rough estimation of the activation energy of lithium motion employing the empirical Waugh–Fedin relation E_A (kJ mol⁻¹) = 0.156 × *T*_{onset} (K).^[38] As onset temperature, the temperature at which the line width is given by (*V*_{rigid lattice} – *V*_{mot. narrowing})/2 was identified. This leads for ω -Li₉TrP₄ with *Tr* = Al, Ga, and In to an approximate onset temperature of 182, 156 and 220K, respectively (Figure 6b,d,f, respectively). In consequence, this results for *Tr* = Al, Ga and In activation energies of 28, 24, and 34 kJ mol⁻¹ (≈ 0.29, 0.25, and 0.35 eV), respectively. Thus, the value for ω -Li₉AlP₄ is higher than that for the β -polymorph (25 kJ mol⁻¹, ≈ 0.26 eV),^[31] but considerably lower than for ω -Li₉InP₄. Overall, the lowest activation energy is found for ω -Li₉GaP₄.

2.5. Impedance Spectroscopy

The Li-ion conductivities of ω -Li₉TrP₄ (*Tr* = Al, Ga, and In) were investigated by impedance measurements in a blocking electrode configuration. The Impedance spectra at different temperatures are displayed in Figure 7a–c. All spectra feature a characteristic high-frequency semicircle and a Warburg-like tail at low frequencies.

The semi-circle can be described as parallel circuit element of a resistor and a constant phase element (*R/Q*), in which *R* represents the total ionic conductivity (Figure 7). To account for the internal capacitance of the cell setup (Figure S14, Supporting Information), the high-frequency regime of the impedance data was fitted with a fixed capacitance of 1.83 × 10⁻¹⁰ F in parallel to the *R/Q* element. This stray capacitance does not affect the determined ion transport properties of the sample. For the constant phase element, the fit of the data acquired at 298 K resulted in α values of ≈ 0.59, 0.59 and 1 and *Q* parameters with values of ≈ 1.6 × 10⁻⁷ F s^(α -1), 2.6 × 10⁻⁷ F s^(α -1) and 1.9 × 10⁻¹⁰ F s^(α -1) for ω -Li₉AlP₄, ω -Li₉GaP₄ and ω -Li₉InP₄, respectively. Applying Brugs formula,^[39] the values of the constant phase elements translate to pseudo capacitances of 1.8 × 10⁻¹⁰ F, 1.7 F × 10⁻¹⁰ and 1.9 × 10⁻¹⁰ F, respectively. The ionic conductivities were determined to be $\sigma_{Li}(\omega\text{-Li}_9\text{AlP}_4) = (1.46 \pm 0.04) \times 10^{-3}$ S cm⁻¹, $\sigma_{Li}(\omega\text{-Li}_9\text{GaP}_4) = (4.5 \pm 0.2) \times 10^{-3}$ S cm⁻¹ and $\sigma_{Li}(\omega\text{-Li}_9\text{InP}_4) = (0.18 \pm 0.01) \times 10^{-3}$ S cm⁻¹ at 298 K. The activation energy for the lithium-ion transport (Figure 7d) was investigated by temperature-dependent impedance measurements in the range between 298 and 358 K, revealing an E_A^{PEIS} of 30 ± 0.5 kJ mol⁻¹ (≈ 0.31 eV) for ω -Li₉AlP₄, an E_A^{PEIS} of 30 ± 0.2 kJ mol⁻¹ (≈ 0.31 eV) for ω -Li₉GaP₄ and an E_A^{PEIS} of 38 ± 0.9 kJ mol⁻¹

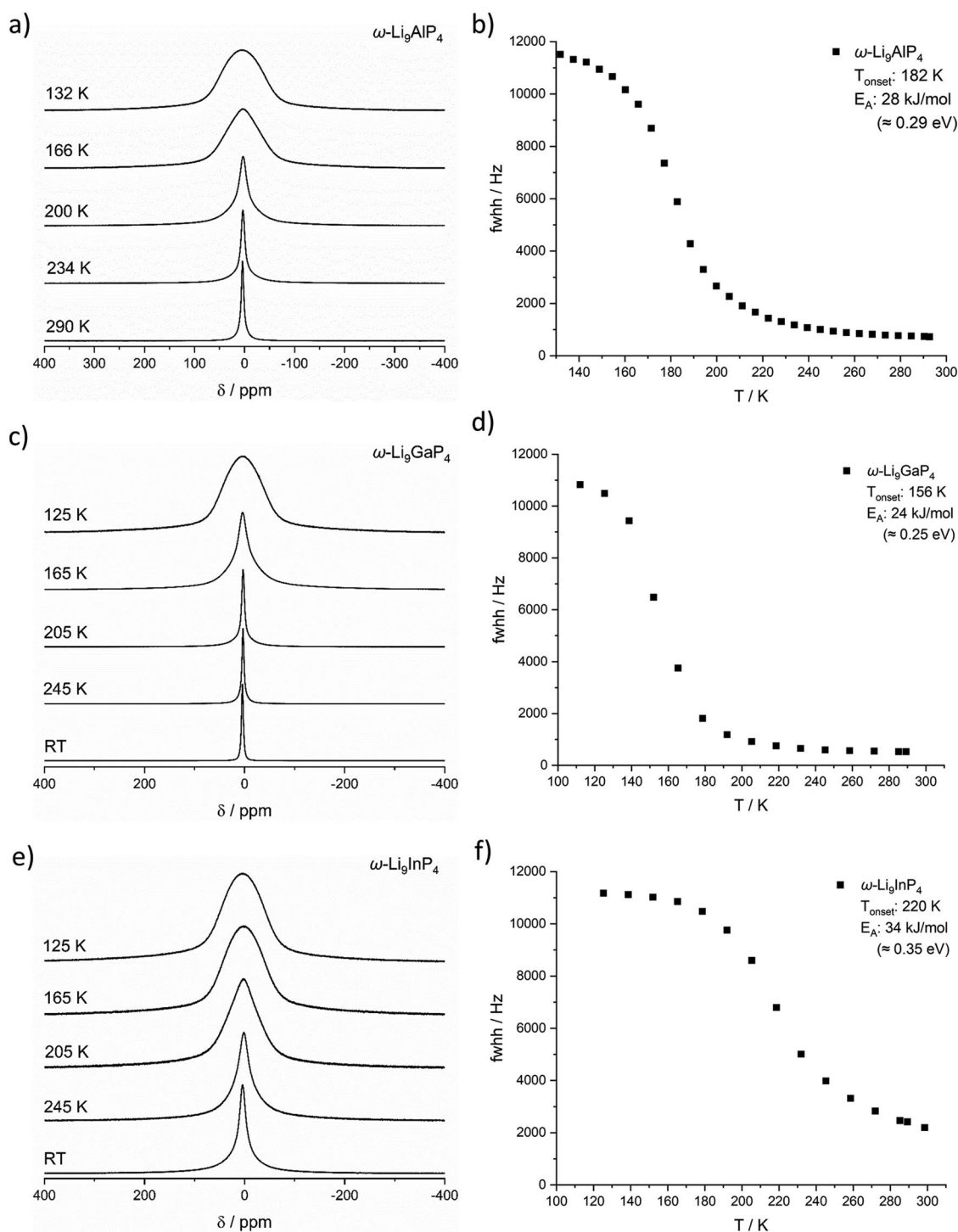


Figure 6. Temperature-dependent evolution of the ⁷Li line shape of a) ω -Li₉AlP₄ recorded in the temperature range from 132 to 290 K and c) ω -Li₉GaP₄ and e) ω -Li₉InP₄ recorded in the temperature range from 125 K to room temperature, respectively. Temperature-dependent linewidth of the ⁷Li signal (full width at half height) of b) ω -Li₉AlP₄, d) ω -Li₉GaP₄, and f) ω -Li₉InP₄.

(\approx 0.39 eV) for ω -Li₉InP₄. DC polarization measurements in the range from 50–150 mV reveal an electronic conductivity of $3.6(9) \times 10^{-8} \text{ S cm}^{-1}$ for ω -Li₉AlP₄, $1.1(5) \times 10^{-7} \text{ S cm}^{-1}$ for ω -Li₉GaP₄ and $2.1(3) \times 10^{-8} \text{ S cm}^{-1}$ for ω -Li₉InP₄ at 298 K (Figure S15, Supporting Information).

2.6. Lithium Diffusion in β -Li₉AlP₄ and ω -Li₉AlP₄ from MEM-Reconstructed Nuclear Scattering Densities

Among all atomic species in Li₉AlP₄, only lithium exhibits a negative scattering length ($b_{\text{Li}} = -1.9 \text{ fm}$) as a sum of

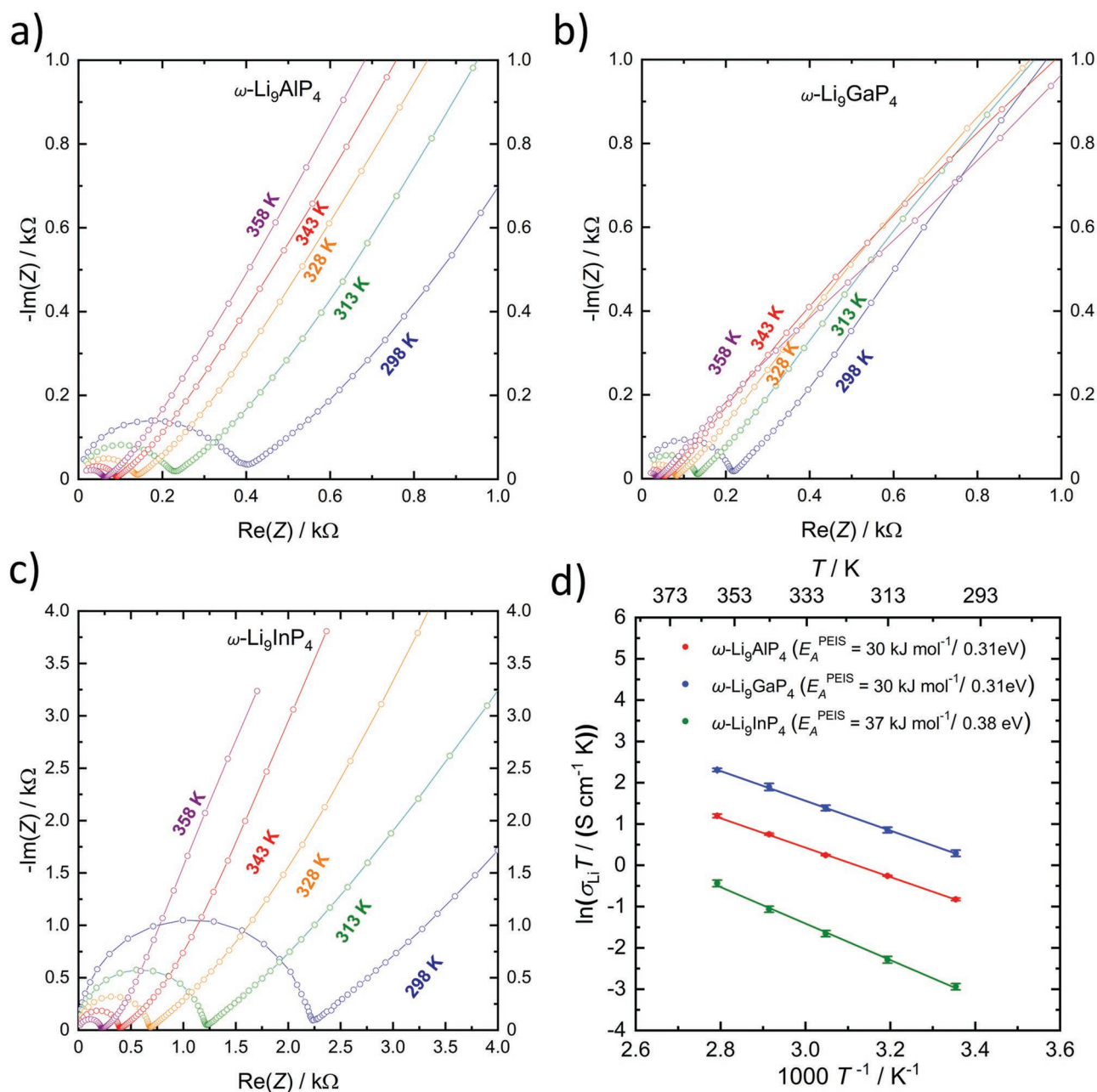


Figure 7. Impedance spectroscopic measurements of $\omega\text{-Li}_9\text{TrP}_4$ ($\text{Tr} = \text{Al, Ga}$ and In) at different temperatures measured under blocking conditions: a) $\omega\text{-Li}_9\text{AlP}_4$, b) $\omega\text{-Li}_9\text{GaP}_4$ and c) $\omega\text{-Li}_9\text{InP}_4$. d) Corresponding Arrhenius plots of the product of conductivity and temperature ($\sigma_{\text{Li}} \times T$) for $\omega\text{-Li}_9\text{TrP}_4$ ($\text{Tr} = \text{Al, Ga}$ and In) obtained in the heating as well as in the cooling branch, with error bars for each measurement based on the standard deviation from independent measurements with three cells; the shown linear fits through both branches was used to obtain the activation energies.

$b(^6\text{Li}) = 2.00 - 0.261i$ fm and $b(^7\text{Li}) = -2.22$ fm with the natural 0.075:0.925 composition. Because of that, and since lithium distribution is under focus, the analysis of nuclear scattering densities can be limited to its negative component. Negative nuclear scattering density maps were calculated from the experimental structure factors measured at 300 and 973 K for $\beta\text{-Li}_9\text{AlP}_4$ and $\omega\text{-Li}_9\text{AlP}_4$, respectively, by constraining the entropy maximization (maximum entropy method). The obtained nuclear densities of $\beta\text{-Li}_9\text{AlP}_4$ were recalculated to one particle potential and

are presented in Figure S16 (Supporting Information) with an isosurface level of 0.21 eV as a threshold.

In $\beta\text{-Li}_9\text{AlP}_4$ there exists a percolating network connecting all lithium atoms. According to the lattice symmetry of $\beta\text{-Li}_9\text{AlP}_4$, it is sufficient to consider the volume in the following region of x, y, z fractional coordinates (0.00–0.50, 0.00–0.50, 0.00–0.50) (Figure 8a). Analysis of Li–Li connectivity yields 21 unique Li–Li interatomic distances with lengths below 3.0 Å (Figure 8b). The pairwise Li connectivity is summarized in Table S14 (Supporting

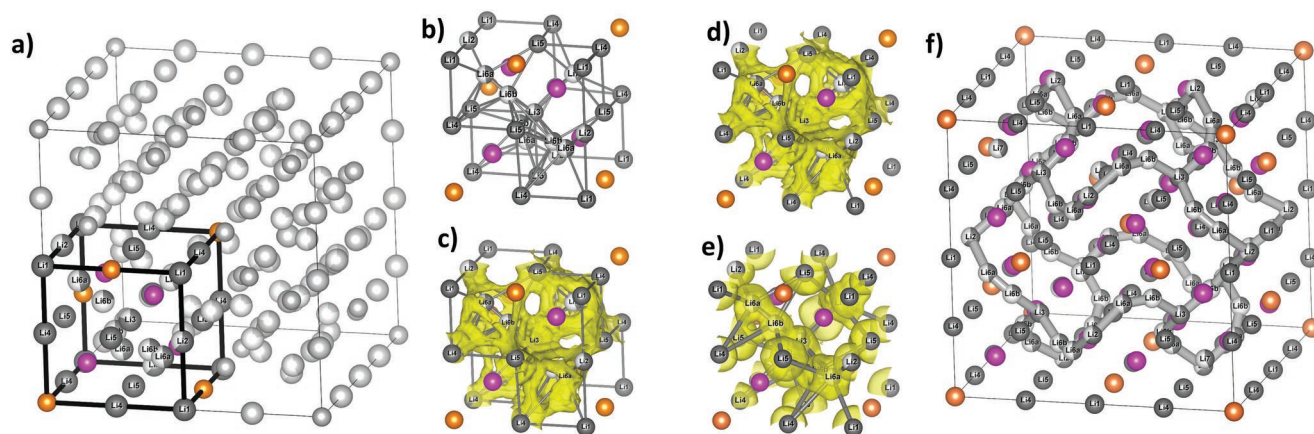


Figure 8. a) Lattice and asymmetric unit in β - Li_9AlP_4 ; b) Li–Li connectivity in the asymmetric unit at 3.0 Å threshold; c) Li–Li connectivity and BVS isosurface ($\Delta V = 0.025$ val. un., yellow); d) filtered Li–Li connectivity and BVS isosurface ($\Delta V = 0.025$ val. un., yellow); e) filtered Li–Li connectivity and negative nuclear scattering densities from MEM reconstruction (isosurface level 0.02 fm \AA^{-3}); f) diffusion pathway of type $-\text{[Li6a-Li6b]}\text{-Li2-[Li6a-Li6b]}\text{-Li3-[Li6a-Li6b]}\text{-}$, determined from OPP analysis. Li atoms are shown as grey spheres, grey bonds correspond to Li–Li interatomic distances.

Information), showing the spread of Li–Li distances from 1.33(5) Å between the disordered Li6 sites (Li6a–Li6b) up to 2.98(3) Å separating Li6a positions. Lithium exchange does not occur over all Li–Li connections (Figure 8c). The rating of pairwise Li connections potentially involved in lithium transport through the β - Li_9AlP_4 lattice was carried out using BVS calculations as a reference, from which a number of closest Li–Li connections was discarded (Figure 8d; Table S14, grey, Supporting Information).

Obtained results were further refined and cross-checked using the analysis of MEM-reconstructed negative nuclear scattering densities and 3D distribution of OPP, corresponding to the energy barriers for Li transport in β - Li_9AlP_4 . OPP was calculated for each type of Li–Li interatomic distance below 3.0 Å and are listed in Table S14 (Supporting Information). Distribution of negative nuclear scattering densities indicated whether Li transport proceeds directly between adjacent Li–Li sites or via dedicated saddle points. Generally, good agreement was noticed between MEM and BVS results (Figure 8e). Evaluation of calculated OPP (Table S14, red, Supporting Information) clearly revealed the favorite diffusion pathways formed by the connectivity of type $-\text{[Li6a-Li6b]}\text{-Li2-[Li6a-Li6b]}\text{-Li3-[Li6a-Li6b]}\text{-}$ (Figure 8f), which are three-dimensionally interconnected with each other (Figure 8b). This pathway involves tetrahedral lithium sites (Li2 and Li3) as well as octahedral lithium sites (Li6a and Li6b). The jumps occur between adjacent tetrahedral and octahedral lithium positions or between the octahedral lithium split positions Li6a and Li6b. This pathway is characterized by three different energy barriers: 0.190 eV for the jump from Li6b to Li3, 0.156 eV for the section Li6a – Li6b and 0.194 eV for section Li2 – Li6a, with a maximum activation barrier of 0.194 eV for the lithium diffusion along the path $-\text{[Li6a-Li6b]}\text{-Li2-[Li6a-Li6b]}\text{-Li3-[Li6a-Li6b]}\text{-}$ (Figure 8f).

Besides the above-mentioned one, there is a number of alternative pathways, which are characterized by slightly lower probabilities. Their majority involves the disordered Li6a – Li6b site, e.g. Li5–Li6a, Li5–Li6b, Li1–Li6a, but at some point, the Li5–Li7 path becomes plausible. In sum, the very good lithium ion conductivity of β - Li_9AlP_4 and MEM calculations suggests an

even lower activation energy of 0.19 eV for lithium diffusion as previously reported by impedance spectroscopy (0.29 eV).^[31] A reason for the discrepancy might be that the impedance spectroscopy only detects effects on the macroscopic scale like grain boundaries and not the activation energy on the atomic scale. On the other hand, the activation barriers calculated via OPP formalism can be underestimated due to non-classical behavior of β - Li_9AlP_4 at 300 K. In general, the slightly smaller activation energies for the ionic conductivity by OPP calculations compared to impedance spectroscopy is a known phenomenon and has also been observed for other compounds such as $\text{Li}_{10}\text{GeP}_2\text{S}_{12}$ ^[40] for which the analysis of the neutron diffraction data also revealed lower activation energies compared to values obtained from impedance measurements.

The distribution of negative nuclear scattering densities for ω - Li_9AlP_4 is presented in Figure 9. The threshold of isosurfaces was set to a value where no artifacts are present corresponding to 0.010 fm \AA^{-3} . At the given threshold the negative nuclear scattering densities are forming a 3D network of lithium atoms indicating a 3D lithium diffusion. Similar to β - Li_9AlP_4 at 300 K the activation energy for jumps of lithium from one tetrahedral site to another (Li1–Li1) and from one tetrahedral site to an octahedral site (Li1–Li2) were estimated from nuclear scattering densities based on OPP formalism. The calculation shows that the lithium hopping between tetrahedral voids is much more favored (0.30 eV) compared to the jumps between tetrahedral and octahedral sites (0.42 eV) (Figure 9). This contradicts the results for $\text{Li}_{14}\text{SiP}_6$ ^[29] where lithium diffusion occurs exclusively via tetrahedral–octahedral hopping with an activation energy of 0.44 eV, whereas in ω - Li_9AlP_4 lithium diffusion can also proceed via edge-sharing tetrahedral voids.

3. Discussion and Conclusions

The recently reported β - Li_9AlP_4 exhibited the highest ionic conductivity of the phosphide-based materials so far. Single crystal X-ray diffraction investigations revealed that β - Li_9AlP_4 features an ordered Cr_3Si -like structure of isolated $[\text{AlP}_4]^{9-}$ tetrahedra

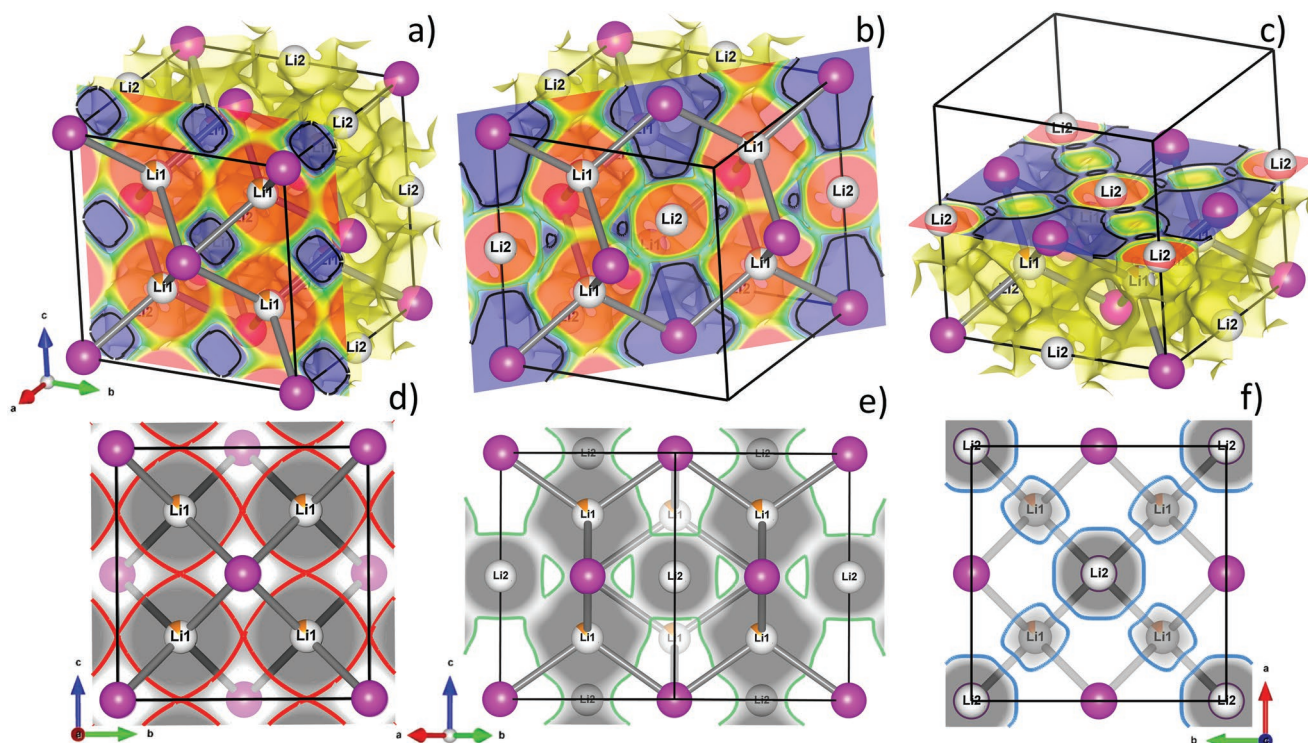


Figure 9. (Top row) Negative nuclear scattering density distribution in ω -Li₉AlP₄ reconstructed from experimental structure factors at 973 K using the maximum entropy method and corresponding 2D section cuts at a) 100, b) 110, and c) 001. Li, P and mixed Al sites are shown as grey, pink and gray/orange spheres, respectively. Black isolines correspond to 0.01 fm⁻³ level. (Bottom row) Calculated plane cuts of OPP distribution at d) 100, e) 110, and f) 001 presented as grayscale, isolines highlight 0.30 eV (red), 0.42 eV (green) and 0.5 eV (blue) levels. The Li1–Li1 and Li1–Li2 exchange represents tetrahedral–tetrahedral and tetrahedral–octahedral jumps, accordingly.

and a highly disordered lithium sublattice with partially occupied lithium positions. Furthermore, the lithium atoms in the octahedral voids are strongly shifted toward triangular faces, and a lithium split position was established. The crystal structure of β -Li₉AlP₄ was now confirmed by powder neutron diffraction. Both, the lithium positions and the lithium site occupation factors from the Rietveld analysis of the powder neutron diffraction experiment at 4 K are in very good accordance with the previously reported structure obtained from single crystal data. The reconstruction of negative nuclear densities, using the MEM approach and their further treatment in the frame of OPP calculations at 300 K, suggest an activation barrier as low as 0.19 eV for a 3D lithium diffusion in β -Li₉AlP₄. The diffusion of the lithium ions occurs preferentially via adjacent tetrahedral and octahedral voids. DSC measurements and temperature-dependent neutron diffraction reveal that ordered β -Li₉AlP₄ undergoes a transformation into the disordered phase ω -Li₉AlP₄ at about 573 K. High-temperature powder neutron and single crystal X-ray diffraction experiments result in approximately half of the lattice parameter of β -Li₉AlP₄. The structure shows a *ccp* of P atoms with Li atoms in the center of the octahedral void, and an aluminum/lithium mixed position in the tetrahedral void and therefore randomly distributed [AlP₄]⁹⁻ tetrahedra. The high-temperature phase ω -Li₉AlP₄ can be synthesized via ball milling of the elements and annealing at 973 K followed by rapid quenching to room temperature. Impedance spectroscopy and temperature-dependent static ⁷Li NMR spectroscopy show

with $\sigma_{\text{Li}} = 1.46(4)$ mS cm⁻¹ at 298 K, an $E_{\text{A}}^{\text{PEIS}} = 0.31$ eV and an $E_{\text{A}}^{\text{NMR}} = 0.29$ eV a slightly poorer conductivity performance for ω -Li₉AlP₄ than for β -Li₉AlP₄ (Table 5).^[31] MEM and OPP calculations from neutron powder refinements at 973 K reveal that lithium diffusion via tetrahedral–tetrahedral jumps is preferred over tetrahedral–octahedral jumps. The reason may be the more symmetric distribution of lithium ions in the lattice, especially in the octahedral void of the high-temperature phase ω -Li₉AlP₄ compared to β -Li₉AlP₄.

The high-temperature modification of the heavier homologs was characterized via powder X-ray diffraction. Both compounds, ω -Li₉GaP₄ and ω -Li₉InP₄, are isotypic to ω -Li₉AlP₄. They crystallize in the Li₃Bi-type in which lithium atoms occupy all of the occurring tetrahedral and octahedral voids. However, ω -Li₉AlP₄, ω -Li₉GaP₄ and ω -Li₉InP₄ have a lower Li content as in Li₃Bi and thus octahedral voids are not fully occupied but reach $\approx 50\%$ occupation. The lattice parameters and volumes as well as the Li1/*T*1–P bond lengths are compared in Table 4.

Considering the compounds ω -Li₉AlP₄, ω -Li₉GaP₄, and ω -Li₉InP₄ as ionic materials, lattice parameters and cell volumes increase from ω -Li₉AlP₄ to ω -Li₉InP₄ as expected from the ionic radii (Al³⁺ 0.53 Å, Ga³⁺ 0.61 Å, In³⁺ 0.76 Å for a coordination number of four, respectively).^[41] The lattice parameters and cell volumes of ω -Li₉AlP₄ and ω -Li₉GaP₄ are very similar, whereas the corresponding values for γ -Li₉InP₄ are significantly larger, which is also observed in the series Li₁₄TtP₆ (*Tt* = Si, Ge, Sn).^[29,30] Interestingly, both Li₉AlP₄ and Li₉GaP₄

Table 4. Lattice parameters, cell volumes and Li1/Tr1–P bond distances in ω -Li₉AlP₄, ω -Li₉GaP₄, and ω -Li₉InP₄ at room temperature.

	<i>a</i> /Å	<i>V</i> /Å ³	<i>d</i> _{Li1/Tr1-P} /Å
ω -Li ₉ AlP ₄	5.94067(4)	209.656(4)	2.5724(1)
ω -Li ₉ GaP ₄	5.94324(9)	209.928(9)	2.5735(1)
ω -Li ₉ InP ₄	6.03378(4)	219.669(5)	2.6127(1)

form an ordered modification (“β”) and a high-temperature disordered modification (“ω”) whereas Li₉InP₄ crystallizes also at moderate temperature and after slow cooling exclusively in the disordered ω modification. It might be that the very similar ionic radii of 0.76 and 0.73 Å for In³⁺ and Li⁺, respectively,^[41] in a coordination number of four stabilizes the disordered ω modification.

According to impedance measurements, ω -Li₉GaP₄ shows with $\sigma_{\text{Li}} = 4.5(2)$ mS cm⁻¹ a new maximum of ionic conductivity of all phosphides so far. The rapid lithium diffusion is supported by a very low activation energy calculated by ⁷Li NMR spectroscopy. Compared to β-Li₉GaP₄, the phase transformation to the disordered ω-modification leads to a better lithium diffusion according to impedance measurements, which is opposite to the trend of ionic conductivity in β/ω-Li₉AlP₄.^[32] To get more insights into the lithium diffusion in ω-Li₉GaP₄ neutron diffraction experiments are scheduled. By contrast, the corresponding indium compound ω-Li₉InP₄ exhibits the so far lowest ionic conductivity of $\sigma_{\text{Li}} = 0.18(1)$ mS cm⁻¹ of the ionic conducting lithium phosphidotrirelates. This is further demonstrated by the highest activation energy of 0.39 eV among the studied samples. Overall, the tendency of the ionic conductivities of ω-Li₉AlP₄, ω-Li₉GaP₄, and ω-Li₉InP₄ is not in correspondence with the increasing lattice parameters. However, the trend is the same as in the structural related Li₁₄TiP₆ (Ti = Si, Ge, Sn) phases, where Li₁₄GeP₆ shows the highest ionic conductivity followed by Li₁₄SiP₆ and Li₁₄SnP₆ (Table 5).

A reason might be the influence of the lattice polarizability on the ionic conductivity, which is quite well known for argyrodites^[42] and was also postulated for the series Li₁₄TiP₆.^[30] where Ge has the smallest difference in electronegativity compared to P and thus the weakest Coulombic Li⁺ ··· P interactions. In case of ω-Li₉AlP₄, ω-Li₉GaP₄, and ω-Li₉InP₄, Ga indeed exhibits the smallest difference in electronegativity compared to P ($\chi(\text{Al}) = 1.47$, $\chi(\text{Ga}) = 1.82$, $\chi(\text{In}) = 1.49$ and $\chi(\text{P}) = 2.06$, Allred–Rochow scale of electronegativity)^[43] and shows the highest conductivity. However, Al and In possess almost the same difference in electronegativity, but In shows a significantly lower conductivity.

Table 5. Comparison of reported ionic conductivities, calculated activation energies from Impedance Spectroscopy, calculated activation energies from temperature-dependent ⁷Li NMR Spectroscopy and the electronic conductivity of several lithium phosphide trielates and tetrelates.^[29–32]

	Li ₁₄ SiP ₆	Li ₁₄ GeP ₆	Li ₁₄ SnP ₆	β-Li ₉ AlP ₄	β-Li ₉ GaP ₄	ω-Li ₉ AlP ₄	ω-Li ₉ GaP ₄	ω-Li ₉ InP ₄
σ_{Li} at RT/mS cm ⁻¹	1.1	1.7	0.93	3.0	1.6	1.5	4.5	0.18
<i>E</i> _A ^{PEIS} /eV	0.33	0.33	0.35	0.29	0.38	0.31	0.31	0.39
<i>E</i> _A ^{NMR} /eV	0.31	0.31	0.29	0.26	0.26	0.29	0.25	0.35
σ_{el} at RT/10 ⁻⁴ mS cm ⁻¹	1.6	1.7	4.1	2.0	2.6	0.36	1.1	0.21

4. Experimental Section

Syntheses, sample preparation, and all manipulations were carried out inside an argon-filled glove box (MBraun, *p*(H₂O), *p*(O₂) < 0.1 ppm). Lithium (Li, rods, Rockwood Lithium, > 99%) was cleaned from oxide layers prior to use. Aluminum (Al, granules, ChemPur, 99,99), indium (In, drops, Sigma–Aldrich, 99.9%), gallium (Ga, pieces, ChemPur, 99,99%), and phosphorus (P_{red}, powder, Sigma–Aldrich, 97%) were used without any further purification.

Synthesis of β-Li₉AlP₄: β-Li₉AlP₄ was synthesized as previously reported from the elements via ball milling and subsequent annealing.^[31] Lithium (1478.8 mg, 213.1 mmol, 9 equiv.), aluminum (632.4 mg, 23.4 mmol, 1 equiv.) and phosphorus (2993.4 mg, 93.7 mmol, 4 equiv.) were ball milled (Retsch PM100 Planetary Ball Mill) for 36 h at 350 rpm with rest periods (every 10 min for 3 min) using a tungsten carbide (WC) milling set (50 mL jar with 3 balls with a diameter of 1.5 cm). The resulting dark-red mixture was pressed into pellets with a diameter of 13 mm for 30 s at 5 t using a hydraulic press (Specac Atlas 15T). The fragmented pellets were filled into graphitized quartz ampoules (8 mm diameter), which were sealed under vacuum with an oxyhydrogen burner. The sealed ampoules were heated in a muffle furnace (Nabertherm P 330) with 5 K min⁻¹ up to 973 K, dwelled for 24 h, and subsequently cooled with 0.5 K min⁻¹ to room temperature. After pestling of the pellets, a brown-yellow powder was obtained.

Single crystals were grown by the reaction of the elements with a slight excess of phosphorus in a tantalum ampoule at 1073 K for 24 h and subsequent cooling with 0.5 K min⁻¹ to room temperature.^[31]

Synthesis of ω-Li₉AlP₄: The first part of the preparation of ω-Li₉AlP₄ was identical with the procedure to prepare the β modification. The fragmented pellets of the pressed dark red powder after ball milling were filled into niobium ampoules which were sealed in an electric arc furnace (Edmund Bühler MAM1). The sealed ampoules were enclosed in evacuated silica reaction containers and heated in a tube furnace (HTM Reetz Loba) with 5 K min⁻¹ up to 973 K, dwelled for 22 h and were rapidly cooled down by quenching directly in an ice/water mixture. After pestling of the pellets, a brown-yellow powder was obtained.

Synthesis of ω-Li₉GaP₄ and ω-Li₉InP₄: ω-Li₉GaP₄ and ω-Li₉InP₄ were synthesized from the elements via ball milling, annealing and subsequent quenching from 973 K. **ω-Li₉GaP₄:** Lithium (861.1 mg, 122.8 mmol, 9.1 equiv.), gallium (943.6 mg, 13.5 mmol, 1.0 equiv.) and phosphorus (1728.2 mg, 54.1 mmol, 4.0 equiv.) were transferred to a WC milling set (45 mL jar, 7 balls with a diameter of 1.5 cm) and ball milled using a Fritsch Pulverisette 6 for 18 h at 350 rpm with resting periods (every 10 min for 5 min). **ω-Li₉InP₄:** Lithium (626.9 mg, 89.0 mmol, 9.0 equiv.), indium (1141.8 mg, 9.9 mmol, 1.0 equiv.), and phosphorus (1269.0 mg, 39.7 mmol, 4.0 equiv.) were transferred to a ZrO₂ milling set (45 mL jar and with 25 balls with a diameter of 1 cm) and ball milled using a Fritsch Pulverisette 6 for 18 h at 350 rpm with resting periods (every 10 min for 5 min). For ω-Li₉GaP₄ a red, and for ω-Li₉InP₄ a red-brown powder was obtained. The powders were pressed into pellets with a diameter of 13 mm for 30 s at 5 t using a hydraulic press (Specac Atlas 15T). The fragmented pellets were filled into niobium ampoules which were sealed in an electric arc furnace (Edmund Bühler MAM1). The sealed ampoules were enclosed in evacuated silica reaction containers and heated in a tube furnace (HTM Reetz Loba) with 5 K min⁻¹ up to 973 K, dwelled for 22 h and were rapidly cooled down by quenching directly in an ice/water

mixture. After pestling of the pellets, a light-red powder was obtained for ω -Li₉GaP₄ and a red-orange powder for ω -Li₉InP₄.

Powder Neutron Diffraction: For powder neutron diffraction measurements, β -Li₉AlP₄ was grounded in an agate mortar inside the glovebox and ≈ 2 cm³ of the respective sample was enclosed in a niobium ampoule (10 mm outer diameter and 0.5 mm wall thickness) and arc-welded under argon. Powder Neutron Diffraction experiments were performed on the high-resolution powder diffractometer SPODI at the research reactor FRM II (Garching, Germany).^[44] Monochromatic neutrons were obtained using (551) reflection of composite and vertically focusing Ge monochromator at 155° take-off angle. Data collection was performed using a multidetector consisting of 80 ³He tubes with 1 inch in diameter and covering an angular range of 160°. The wavelength $\lambda = 1.5482$ Å was determined using reflection positions of Si reference. Data collection was performed at ambient temperature and at low temperatures the closed-cycle refrigerator was utilized (⁴He as heat transmitter); high-temperature studies were carried out using vacuum furnace.

Rietveld Analyses of Powder Neutron Data: Rietveld refinements of β -Li₉AlP₄ at 4 and 300 K as well as ω -Li₉AlP₄ at 973 K were performed with the FullProf program package.^[45] Relatively high symmetric β -Li₉AlP₄ limits the number of observed reflections, which along with the strong signal from the Nb holder and a high neutron absorption of $\mu_R = 1.5$ constrained the model. The analysis started with the dataset collected at 4 K, where lattice parameters and fractional atomic coordinates were refined independently. During the simultaneous refinement of displacement parameters and site occupation factors, a number of parameter correlations were observed. In order to avoid/minimize them, isotropic displacement parameters were constrained as follows: B(Al1) = B(Al2), B(P1) = B(P2), B(Li1), B(Li4), B(Li2) = B(Li3) = B(Li5) = B(Li6a) = B(Li6b) = B(Li7). Obtained site occupations for Li1, Li4, and Li5 have been found close to 100% and, therefore, corresponding sites were kept fully occupied. Site occupations at Li2, Li3, Li6a – Li6b and Li7 were refined at 4 K. The structural model at 300 K was refined using 4 K data as an input. Lattice parameters and fractional coordinates were freely refined in accordance with the symmetry, site occupations were fixed to values determined at 4 K. Constraints for displacement parameters at Al and P sites remained unchanged. At the Li sites the isotropic displacement parameters were applied according to the following scheme, minimizing parameter correlations: B(Li1), B(Li2), B(Li3), B(Li4), B(Li5), B(Li6a) = B(Li6b), B(Li7).

During Rietveld refinement of ω -Li₉AlP₄ at 973 K cell parameters, fractional atomic coordinates and isotropic displacement parameters were refined independently. For the mixed position Li1/Al1 at the tetrahedral position 8c, a coupled displacement parameter was used and a full occupancy by Li1/Al1 was assumed. Due to low parameter to observables ratio, the site occupancy factors of lithium to aluminum (Li1, Al1, and Li2) were fixed according to the expected formula Li₉AlP₄. The assumption of the formula relies on the stoichiometry used for the synthesis and that no side phase is observed by neutron diffraction. Further details of the crystal structure investigations may be obtained from the joint CCDC/FIZ Karlsruhe online deposition service: <https://www.ccdc.cam.ac.uk/structures/?> by quoting the deposition numbers CSD-2121625 (β -Li₉AlP₄, 4 K), CSD-2121626 (β -Li₉AlP₄, 300 K), and CSD-2121627 (ω -Li₉AlP₄, 973 K).

Analysis of Differential Bond-Valence Sums (BVS): 3D differential bond-valence sums were generated using the method proposed by Adams,^[46] where the cell volume was represented by 60×60×60 voxels of 0.1 Å³. Structural information from the P and Al framework obtained from Rietveld refinement was used as an input, the differential bond valences were calculated using $R_0 = 1.47867$ Å and $b = 0.724$ bond valence parameters at 7.0 Å cut-off.^[47]

Analysis of Nuclear Densities Using Maximum Entropy: Reconstruction of nuclear densities was performed by maximum entropy method (MEM) as implemented in the program Dynomia.^[48] It was based on the estimation of 3D scattering densities from a limited amount of information by maximizing information entropy under restraints and the results of Rietveld refinement were used as an input. 3D distribution

of nuclear scattering densities was generated on a 128×128×128 grid sampling the cell volume. Activation energies were determined using the connectivity of nuclear densities and their analyses in single/one particle potential (OPP) approximation.^[49] All data visualizations of bond-valence and MEM calculations were performed using the program Vesta.^[50,51]

Single Crystal Structure Determination: A single crystal of β -Li₉AlP₄ was sealed in a 0.3 mm glass capillary. The single crystal X-ray diffraction (SCXRD) measurement was carried out on a STOE Stadivari diffractometer equipped with a Ge(111) monochromator, Mo K α radiation ($\lambda = 0.71073$ Å) source, a DECTRIS PILATUS3R 300 K detector and a heating unit. The measurement was performed at 553 K. The structure was solved by Direct Methods (SHELXS) and refined by full-matrix least-squares calculations against F^2 (SHELXL).^[52] According to the structure refinement by neutron powder data, the site occupation factors of Li1, Al1, and Li2 were fixed according to the formula Li₉AlP₄. Details of the single crystal structure investigation may be obtained via <https://www.ccdc.cam.ac.uk/structures/?> by quoting the deposition number CSD-2121624.

Powder X-Ray Diffraction: For powder X-ray diffraction (PXRD) measurements, the samples were grounded in an agate mortar and sealed inside 0.3 mm glass capillaries. PXRD measurements were performed at room temperature on a STOE Stadi P diffractometer equipped with a Ge(111) monochromator for Cu K α radiation ($\lambda = 1.54056$ Å) or Mo K α radiation ($\lambda = 0.7093$ Å) and a Dectris MYTHEN DCS 1K solid-state detector. The raw powder data were processed with the software package WinXPOW.^[53]

Rietveld Analysis of Powder X-Ray Data: Rietveld refinements were performed with TOPAS V6.^[54] The structure solution of ω -Li₉AlP₄ from neutron powder data was used as the structural model. The mixed occupied positions Li1/Tr1 ($Tr = Al, Ga, In$) were refined with a joint isotropic displacement parameter. All site occupancy factors were refined freely for ω -Li₉GaP₄ and ω -Li₉InP₄. For ω -Li₉AlP₄ the site occupancies of Li1/Al1 were fixed according to the ratio of 1:4 of Al and P. The restraint for position Li1/Tr1 was that the position is in sum fully occupied. Further details of the crystal structure investigations have been deposited at the joint CCDC/FIZ Karlsruhe service under CSD-2121628 (ω -Li₉AlP₄), CSD-2121629 (ω -Li₉GaP₄), and CSD-2121630 (ω -Li₉InP₄).

Differential Scanning Calorimetry (DSC): For thermal analysis, the samples were sealed in niobium ampoules and measured on a DSC instrument (Netzsch, DSC 404 Pegasus) under a constant gas flow of 75 mL min⁻¹. The samples were heated to 1023 K and then cooled to 423 K twice at a rate of 10 °C min⁻¹. For the determination of the onset temperatures of the DSC signals, the PROTEUS Thermal Analysis software was used.^[55]

Impedance Spectroscopy: The ionic conductivities of ω -Li₉TrP₄ ($Tr = Al, Ga, In$) were determined by electrochemical impedance spectroscopy (EIS) in an in-house designed cell.^[29] Three measurements were performed using the same batch for each phase. Powdered samples of ω -Li₉AlP₄ (200 mg), ω -Li₉GaP₄ (400 mg), and ω -Li₉InP₄ (200 mg) were placed between two 8 mm dies, and the screws were fastened with a torque of 30 Nm, respectively, compressing the samples to $\approx 94\%$ (ω -Li₉AlP₄), $\approx 85\%$ (ω -Li₉GaP₄) and $\approx 85\%$ (ω -Li₉InP₄) of their crystal density. Impedance spectra were recorded on a Bio-Logic potentiostat (VSP-300) in a frequency range from 7 to 50 mHz at a potential perturbation of ± 10 mV. Data were treated using the software EC-Lab (V 11.27). The measurements were performed in an Ar-filled glove box at 298 K. The electronic conductivities were determined with the same setup using a potentiostatic polarization procedure, applying voltages of 50, 100, and 150 mV for 7 h each. For determining the activation energies of lithium-ion conduction, the cell temperature was set to 298, 313, 328, 343, and 358 K using an in-house designed temperature casing that is connected to a thermostat (Julabo, F 25). Prior to EIS measurements, the cell rested for 120 min to allow for thermal equilibration. EIS measurements were performed at both heating and cooling cycles.

⁷Li Static Temperature-Dependent NMR Spectroscopy: Low-temperature ⁷Li NMR measurements had been performed at a 7.04 T Bruker Avance 3 spectrometer equipped with a 4 mm-MAS-WVT-Probe. The resonance frequency of ⁷Li at this field strength was 116.64 MHz. For

temperature-dependent static ^7Li spectra, the sample had been enclosed in a glass-ampoule to avoid contact with air and moisture. A saturation comb had been used prior to data acquisition, and a relaxation delay between 30 and 1 s and 4 repetitions had been typically used. The spectra were referenced to a 9.7 molar LiCl-solution. Temperature calibration had been performed by measuring the temperature-dependent chemical shift of lead nitrate, $\text{Pb}(\text{NO}_3)_2$, which had been enclosed in a glass ampoule as well.

Supporting Information

Supporting Information is available from the Wiley Online Library or from the author.

Acknowledgements

The authors are grateful to the Bavarian Ministry of Economic Affairs, Regional Development, and Energy for funding their research in the project “Industrialisierbarkeit von Festkörperelektrolytzellen”. The authors thank C. Sedlmeier as well as H. A. Gasteiger for valuable discussion on the cell setup.

Open access funding enabled and organized by Projekt DEAL.

Conflict of Interest

The authors declare no conflict of interest.

Data Availability Statement

The data that support the findings of this study are available in the supplementary material of this article.

Keywords

batteries, ion migration, solid ion conductors, structures, synthesis

Received: December 3, 2021

Revised: August 8, 2022

Published online: September 7, 2022

- [1] P. Knauth, *Solid State Ionics* **2009**, *180*, 911.
- [2] Z. Zhang, Y. Shao, B. Lotsch, Y.-S. Hu, H. Li, J. Janek, L. F. Nazar, C.-W. Nan, J. Maier, M. Armand, L. Chen, *Energy Environ. Sci.* **2018**, *11*, 1945.
- [3] Y.-S. Hu, *Nat. Energy* **2016**, *1*, 16042.
- [4] J. Janek, W. G. Zeier, *Nat. Energy* **2016**, *1*, 16141.
- [5] Z. Gao, H. Sun, L. Fu, F. Ye, Y. Zhang, W. Luo, Y. Huang, *Adv. Mater.* **2018**, *30*, 1705702.
- [6] J. C. Bachman, S. Muy, A. Grimaud, H.-H. Chang, N. Pour, S. F. Lux, O. Paschos, F. Maglia, S. Lupart, P. Lamp, L. Giordano, Y. Shao-Horn, *Chem. Rev.* **2016**, *116*, 140.
- [7] Y. Meesala, A. Jena, H. Chang, R.-S. Liu, *ACS Energy Lett.* **2017**, *2*, 2734.
- [8] P. Bron, S. Johansson, K. Zick, J. Schmedt auf der Günne, S. Dehnen, B. Roling, *J. Am. Chem. Soc.* **2013**, *135*, 15694.
- [9] J. M. Whiteley, J. H. Woo, E. Hu, K.-W. Nam, S.-H. Lee, *J. Electrochem. Soc.* **2014**, *161*, A1812.
- [10] A. Kuhn, O. Gerbig, C. Zhu, F. Falkenberg, J. Maier, B. V. Lotsch, *Phys. Chem. Chem. Phys.* **2014**, *16*, 14669.
- [11] A. Kuhn, V. Duppel, B. V. Lotsch, *Energy Environ. Sci.* **2013**, *6*, 3548.
- [12] E. Rangasamy, Z. Liu, M. Gobet, K. Pilar, G. Sahu, W. Zhou, H. Wu, S. Greenbaum, C. Liang, *J. Am. Chem. Soc.* **2015**, *137*, 1384.
- [13] S. Harm, A.-K. Hatz, I. Moudrakovski, R. Eger, A. Kuhn, C. Hoch, B. V. Lotsch, *Chem. Mater.* **2019**, *31*, 1280.
- [14] H. Yamane, M. Shibata, Y. Shimane, T. Junke, Y. Seino, S. Adams, K. Minami, A. Hayashi, M. Tatsumisago, *Solid State Ionics* **2007**, *178*, 1163.
- [15] Y. Kato, S. Hori, T. Saito, K. Suzuki, M. Hirayama, A. Mitsui, M. Yonemura, H. Iba, R. Kanno, *Nat. Energy* **2016**, *1*, 16030.
- [16] K. Homma, M. Yonemura, T. Kobayashi, M. Nagao, M. Hirayama, R. Kanno, *Solid State Ionics* **2011**, *182*, 53.
- [17] M. Tachez, J.-P. Malugani, R. Mercier, G. Robert, *Solid State Ionics* **1984**, *14*, 181.
- [18] H. J. Deiseroth, S. T. Kong, H. Eckert, J. Vannahme, C. Reiner, T. Zaiß, M. Schlosser, *Angew. Chem., Int. Ed.* **2008**, *47*, 755.
- [19] S. Boulineau, M. Courty, J.-M. Tarascon, V. Viallet, *Solid State Ion* **2012**, *221*, 1.
- [20] V. Epp, Ö. Gün, H.-J. Deiseroth, M. Wilkening, *J. Phys. Chem. Lett.* **2013**, *4*, 2118.
- [21] N. Kamaya, K. Homma, Y. Yamakawa, M. Hirayama, R. Kanno, M. Yonemura, T. Kamiyama, Y. Kato, S. Hama, K. Kawamoto, A. Mitsui, *Nat. Mater.* **2011**, *10*, 682.
- [22] R. Kanno, T. Hata, Y. Kawamoto, M. Irie, *Solid State Ionics* **2000**, *130*, 97.
- [23] M. Murayama, R. Kanno, M. Irie, S. Ito, T. Hata, N. Sonoyama, Y. Kawamoto, *J. Solid State Chem.* **2002**, *168*, 140.
- [24] Z. Liu, W. Fu, E. A. Payzant, X. Yu, Z. Wu, N. J. Dudney, J. Kiggans, K. Hong, A. J. Rondinone, C. Liang, *J. Am. Chem. Soc.* **2013**, *135*, 975.
- [25] R. Kanno, M. Murayama, *J. Electrochem. Soc.* **2001**, *148*, A742.
- [26] L. Toffoletti, H. Kirchhain, J. Landesfeind, W. Klein, L. van Wüllen, H. A. Gasteiger, T. F. Fässler, *Chem. - Eur. J.* **2016**, *22*, 17635.
- [27] H. Eickhoff, S. Strangmüller, W. Klein, H. Kirchhain, C. Dietrich, W. G. Zeier, L. van Wüllen, T. F. Fässler, *Chem. Mater.* **2018**, *30*, 6440.
- [28] S. Strangmüller, H. Eickhoff, W. Klein, G. Raudaschl-Sieber, H. Kirchhain, T. Kutsch, V. Baran, A. Senyshyn, L. van Wüllen, H. A. Gasteiger, T. F. Fässler, *J. Mater. Chem. A* **2021**, *9*, 15254.
- [29] S. Strangmüller, H. Eickhoff, D. Müller, W. Klein, G. Raudaschl-Sieber, H. Kirchhain, C. Sedlmeier, V. Baran, A. Senyshyn, V. L. Deringer, L. van Wüllen, H. A. Gasteiger, T. F. Fässler, *J. Am. Chem. Soc.* **2019**, *141*, 14200.
- [30] S. Strangmüller, H. Eickhoff, G. Raudaschl-Sieber, H. Kirchhain, C. Sedlmeier, L. van Wüllen, H. A. Gasteiger, T. F. Fässler, *Chem. Mater.* **2020**, *32*, 6925.
- [31] T. M. F. Restle, C. Sedlmeier, H. Kirchhain, W. Klein, G. Raudaschl-Sieber, V. L. Deringer, L. v. Wüllen, H. A. Gasteiger, T. F. Fässler, *Angew. Chem., Int. Ed.* **2020**, *59*, 5665.
- [32] T. M. F. Restle, C. Sedlmeier, H. Kirchhain, W. Klein, G. Raudaschl-Sieber, L. v. Wüllen, T. F. Fässler, *Chem. Mater.* **2021**, *33*, 2957.
- [33] A. Haffner, T. Bräuniger, D. Johrendt, *Angew. Chem.* **2016**, *128*, 13783.
- [34] H. Eickhoff, L. Toffoletti, W. Klein, G. Raudaschl-Sieber, T. F. Fässler, *Inorg. Chem.* **2017**, *56*, 6688.
- [35] H. Eickhoff, C. Sedlmeier, W. Klein, G. Raudaschl-Sieber, H. A. Gasteiger, T. F. Fässler, *Z. Anorg. Allg. Chem.* **2020**, *646*, 95.
- [36] T. M. F. Restle, J. V. Dums, G. Raudaschl-Sieber, T. F. Fässler, *Chem. - Eur. J.* **2020**, *26*, 6812.
- [37] T. M. F. Restle, V. L. Deringer, J. Meyer, G. Raudaschl-Sieber, T. F. Fässler, *Chem. Sci.* **2021**, *12*, 1278.
- [38] J. S. Waugh, E. I. Fedin, *Phys. Solid State* **1963**, *4*, 1633.
- [39] G. J. Brug, A. L. G. v Eeden, M. S.-. Rehbach, J. Sluyters, *J. Electroanal. Chem.* **1984**, *176*, 275.

- [40] D. A. Weber, A. Senyshyn, K. S. Weldert, S. Wenzel, W. Zhang, R. Kaiser, S. Berendts, J. Janek, W. G. Zeier, *Chem. Mater.* **2016**, *28*, 5905.
- [41] R. D. Shannon, *Acta Crystallogr. A* **1976**, *32*, 751.
- [42] M. A. Kraft, S. P. Culver, M. Calderon, F. Böcher, T. Krauskopf, A. Senyshyn, C. Dietrich, A. Zevalkink, J. Janek, W. G. Zeier, *J. Am. Chem. Soc.* **2017**, *139*, 10909.
- [43] A. L. Allred, E. G. Rochow, *J. Inorg. Nucl. Chem.* **1958**, *5*, 264.
- [44] M. Hoelzel, A. Senyshyn, O. Dolotko, *Journal of Large-Scale Research Facilities JLSRF* **2015**, *1*, A5.
- [45] J. Rodriguez-Carvajal, J. Gonzales-Platas, *FullProf Suite 2. 05*, Institute Laue-Langevin, Grenoble, France, **2011**.
- [46] S. Adams, *Acta Cryst. B* **2001**, *57*, 278.
- [47] H. Chen, S. Adams, *IUCr* **2017**, *4*, 614.
- [48] K. Momma, T. Ikeda, A. A. Belik, F. Izumi, *Powder Diffr.* **2013**, *28*, 184.
- [49] A. Senyshyn, H. Boysen, R. Niewa, J. Banys, M. Kinka, Y. Burak, V. Adamiv, F. Izumi, I. Chumak, H. Fuess, *J. Phys. D Appl. Phys.* **2012**, *45*, 175305.
- [50] K. Momma, F. Izumi, *J. Appl. Cryst.* **2011**, *44*, 1272.
- [51] H. Stöfler, T. Zinkevich, M. Yavuz, A. Senyshyn, J. Kulisch, P. Hartmann, T. Aderman, S. Randau, F. H. Richter, J. Janek, S. Indris, H. Ehrenberg, *J. Phys. Chem. C* **2018**, *112*, 15954.
- [52] G. Sheldrick, *Acta Crystallogr., Sect. C: Struct. Chem.* **2015**, *71*, 3.
- [53] WinXPOW, 3.0.2.1, STOE & Cie GmbH Darmstadt, Germany, **2011**.
- [54] TOPAS, 6, Bruker AXS, **2016**.
- [55] PROTEUS Thermal Analysis V4.8.2, Netzsch-Gerätebau GmbH, Selb, **2006**.